
The manuscript is a preprint and has been submitted for publication in JGR: Solid Earth. Please note that the manuscript has not undergone peer review. Subsequent versions of this manuscript may have different content. If accepted, the final version of this manuscript will be available via the 'Peer-reviewed Publication DOI' link on the right-hand side of this webpage. Please feel free to contact any of the authors. We welcome feedback!

1 **The influence of mantle structure on dynamic**
2 **topography in southern Africa**

3 **Kenneth C. Gourley¹ and Christopher Harig¹**

4 ¹Department of Geosciences, University of Arizona, Tucson, AZ, USA

5 **Key Points:**

- 6 • We generate Bayesian estimates of localized radial mantle viscosity and dynamic
7 topography in southern Africa
- 8 • We model present-day vertical displacement of southern African using GNSS sta-
9 tion timeseries and Slepian localization techniques
- 10 • There is evidence for significant dynamic support ($> 1000\ m$) and present-day ver-
11 tical displacement ($1.5\ mm/yr$) due to mantle dynamics

Corresponding author: K. Gourley, kengourley@arizona.edu

12 **Abstract**

13 Due to relatively high terrain and negligible active tectonics, the southern Africa region
14 boasts over thirty independent estimates of dynamic topography. These published es-
15 timates display a wide variance due to both the variety of methods used in computation
16 and a lack of constraints on the regional mantle structure. Here we show that a focus
17 on regional mantle structure is important to generate accurate models of dynamics and
18 dynamic topography. Global average mantle properties are not representative of a par-
19 ticular region, and it is necessary to generate viscosity profiles specific to a region of in-
20 terest. We develop a Bayesian inversion using dynamic geoid kernels, existing seismic
21 tomography models, and Slepian functions to invert for a localized radial viscosity pro-
22 file that best explains the geoid in southern Africa. With an understanding of viscosity
23 uncertainty, we place constraints on the amount of dynamic topography in southern Africa
24 to between 1000 and 2000 *m*. Additionally, we model vertical displacements from 112
25 GNSS stations across our region to examine the long-term, long wavelength pattern of
26 present-day vertical motion, revealing that up to 1.5 *mm/yr* of vertical motion can be
27 explained by ongoing dynamic topography. Our study demonstrates the utility of dy-
28 namic geoid kernels in local nonlinear inversions of non-unique geophysical data. Fur-
29 thermore, we present evidence that there the mantle beneath southern Africa is gener-
30 ating significant dynamic support for and vertical displacement of the lithosphere in this
31 region.

32 **Plain Language Summary**

33 The high topography of southern African is a result of the interaction between the
34 lithosphere and the mantle beneath the region, a process referred to as dynamic topog-
35 raphy. The viscosity of Earth’s mantle is a primary driver of the buoyancy forces that
36 generate this dynamic topography. There is significant disagreement regarding the am-
37 plitude and pattern of dynamic topography in this region, partially owing to the lack of
38 constraints on inputs to geodynamic models, especially viscosity. We use the geoid to
39 constrain mantle viscosity within our study region by combining existing statistical tech-
40 niques in a novel manner. We generate models of mantle viscosity, dynamic topography,
41 and present-day vertical displacement for our study region. Our preferred model results
42 in 1000–2000 meters of dynamic topography, suggesting that the whole of southern Africa
43 is dynamically supported. We also find evidence that present-day vertical displacement

44 is at or exceeds 1.5 mm/yr throughout most of the region, suggesting that dynamic to-
45 pography is currently increasing in this region. We argue that the viscosity within any
46 given region of the mantle differs significantly from the whole-mantle average, and care
47 must be taken to use a viscosity model that corresponds to the region of interest when
48 creating geodynamic models.

49 **1 Introduction**

50 Convective forces and motions within Earth’s mantle cause deformation of the litho-
51 sphere and the surface, the most well-known expression of this process being plate tec-
52 tonics. These forces also cause vertical displacement of Earth’s surface, commonly termed
53 dynamic topography (Forte et al., 1993; Morgan, 1965a,b; M. A. Richards & Hager, 1984).
54 For the purposes of this study, we define dynamic topography similar to Molnar et al.
55 (2015): the surface deformation due to normal tractions applied at the base of the litho-
56 sphere. This definition includes a narrower set of mantle processes than those employed
57 by other studies (e.g. Holdt et al., 2022; Moucha & Forte, 2011), who allow buoyancy
58 variations within the lithosphere to influence their prediction of dynamic topography.
59 We consider such processes static and instead wish to focus on surface deflection due to
60 mantle flow.

61 Southern Africa has been the subject of significant focus as a region with possible
62 dynamic topography. Despite a definitive lack of recent tectonic activity in this region,
63 the Southern African Plateau exists at a relatively high mean elevation of almost 1000 m
64 (Al-Hajri et al., 2009) (Figure 1(a)). This region has been devoid of active orogeny, sub-
65 duction, and widespread volcanics for tens of millions of years (Pasyanos & Nyblade, 2007),
66 yet significant removal of crustal material has occurred during the same time frame (de
67 Wit, 2007). The combination of these factors has led many to draw the conclusion that
68 the mantle must contribute to the plateau elevation.

69 The geoid over southern Africa (Figure 1(b)) gives a sense of the isostatic contri-
70 bution to surface topography (Colli et al., 2016; Molnar et al., 2015; Ricard et al., 1984).
71 Given that the range of geoid values is low in this region, the lithosphere does not con-
72 tribute much to the observed signal. Thus, the isostatic contribution to the overall am-
73 plitude of surface topography is fairly low (Morgan, 1965a). This lends support to the

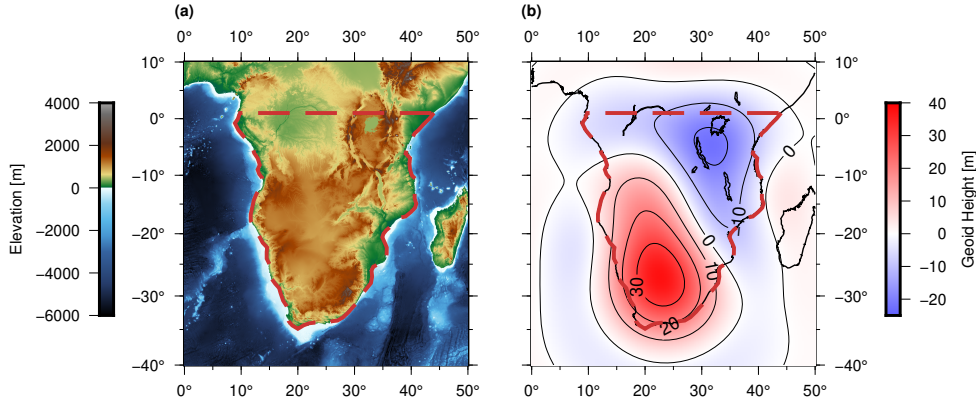


Figure 1. Maps of southern Africa showing (a) the topography and bathymetry of the region from ETOPO1 (Amante & Eakins, 2009); and (b) the non-hydrostatic geoid from EGM2008 (Pavlis et al., 2012) localized using Slepian techniques (see Section 2.2). The red dashed line in both maps denotes the outline of the study region. As shown in (a), the plateau in our study region has around 1000 *m* mean elevations, with some parts extending up to 2000 *m* in elevation. Meanwhile, the geoid in (b) remains relatively low within this same region.

74 idea that there is a moderate to large component of dynamic support in southern Africa
 75 (e.g. Flament et al., 2013; Lithgow-Bertelloni & Silver, 1998)).

76 Over 25 studies performed over the past four decades have made predictions about
 77 the amplitude of dynamic topography in southern Africa. While most of these studies
 78 are through global geodynamic modelling, several focus on regional analyses in south-
 79 ern Africa. Despite the amount of attention the region has received, the results have yet
 80 to converge to a consensus range of possible dynamic topography values. These predic-
 81 tions span a wide range: 0 *m* (Forte et al., 2010), 200 *m* (Molnar et al., 2015), 300 *m*
 82 (Zhang et al., 2012), 300–600 *m* (Gurnis et al., 2000), 650–700 *m* (Lithgow-Bertelloni
 83 & Silver, 1998), and greater than 1200 *m* (Flament et al., 2014). The significant disagree-
 84 ment between these estimates stems primarily from a lack of data in southern Africa.
 85 The region has both poor seismic station coverage and very few large seismic events, re-
 86 sulting in under-constrained tomographic images of the mid- to upper-mantle (Fishwick,
 87 2010). Likewise, not enough receiver function and tectonic studies have been performed
 88 in southern Africa to provide conclusive data about density within the lithosphere (Sun

89 et al., 2018). Without the proper data to constrain geodynamic inversions, the variance
90 between studies remains high.

91 Here, we use the non-hydrostatic geoid as a constraint to invert for the viscosity
92 of the mantle beneath southern Africa using Bayesian statistical analyses of instanta-
93 neous flow models. These inversions also result in estimates of dynamic topography that
94 result from the mantle flow models. Additionally, we examine vertical Global Naviga-
95 tion Satellite System (GNSS) station motions, which we localize within southern Africa
96 using Slepian functions. Our results are applicable to understanding the structure of the
97 mantle beneath southern Africa, including that of the African large low-shear-velocity
98 province (LLSVP), and how it influences mantle-induced surface deformation.

99 **2 Methods**

100 We use instantaneous geodynamic modeling and geoid constraints to invert for the
101 mantle radial viscosity structure. We combine spatio-spectral localization (Simons et al.,
102 2006) with Bayesian statistical techniques (Sambridge et al., 2013) to compute both global
103 and regional mantle viscosity profiles. Together, this analysis gives an informed estimate
104 of the magnitude of dynamic topography in southern Africa. In addition, we generate
105 an estimate of the current vertical displacement in southern Africa by inverting GNSS
106 vertical station data.

107 **2.1 Geoid and Surface Displacement Kernels**

108 Following the method of Hager & Clayton (1989), we construct Green’s functions
109 that map mantle viscosity and density to surface observables. These kernels produce dy-
110 namic models of both the geoid and dynamic topography at the Earth’s surface. The
111 derivation of these Green’s functions is briefly outlined below.

112 In order to calculate the deformation related to dynamics and the resulting geoid,
113 we need to solve the equations of motion. These equations include self-gravitation and
114 assume there is no hydrostatic reference stress or potential. Additionally, coupling be-
115 tween poloidal and toroidal components of flow is ignored, because lateral viscosity vari-
116 ations are assumed to be insignificant. We contend that this is case for our regional anal-
117 yses, where any heterogeneities in the mantle below southern Africa are likely to be small
118 (Yang & Gurnis, 2016). We approximate the vertically heterogeneous mantle as a stack

119 of homogeneous shell layers and solve the system by a propagator matrix technique to
 120 obtain the kernels. No-slip boundary conditions are applied between layers, and free-slip
 121 boundary conditions are applied at the Earth’s surface and the core-mantle boundary
 122 (CMB).

123 Once these kernels are constructed, we linearly convolve the response function with
 124 a density model of the mantle to determine the total field. The potential field at the sur-
 125 face R is defined as

$$\mathcal{V}_{lm}(\mathbf{R}) = \frac{4\pi GR}{2l+1} \int_c^R \mathcal{G}^l(r) \delta\rho_{lm}(r) dr. \quad (1)$$

126 Here, $\mathcal{V}_{lm}(\mathbf{R})$ is the anomalous potential at the Earth’s surface; r is the radial coordi-
 127 nate; l is the spherical harmonic degree; m is the spherical harmonic order; G is the grav-
 128 itational constant; c is the CMB; $\mathcal{G}^l(r)$ is the geoid kernel, and $\delta\rho_{lm}(r)$ is the perturbed
 129 density model of the mantle as a function of depth. The displacement field at the sur-
 130 face is similarly defined as

$$H_{lm}(\mathbf{R}) = \frac{1}{\Delta\rho_R} \int_c^R \mathcal{A}^l(r) \delta\rho_{lm}(r) dr. \quad (2)$$

131 $H_{lm}(\mathbf{R})$ is the deformation at the Earth’s surface; $\mathcal{A}^l(r)$ is the surface displacement ker-
 132 nel; and $\Delta\rho_R$ is the average density of the mantle. $\mathcal{V}_{lm}(\mathbf{R})$, $H_{lm}(\mathbf{R})$, and $\delta\rho_{lm}(r)$ are
 133 functions of spherical harmonic degree l and order m , while the geoid $\mathcal{G}^l(r)$ and surface
 134 displacement $\mathcal{A}^l(r)$ kernels are functions only of spherical harmonic degree.

135 We show geoid and surface displacement kernels for two simple models of the man-
 136 tle’s radial viscosity (Figure 2). This method of mapping a mantle density structure to
 137 an instantaneous geoid and dynamic topography is computationally faster than time-
 138 dependent analytical models (e.g. Le Stunff & Ricard, 1997) and more precise than other
 139 instantaneous flow models (e.g. Lithgow-Bertelloni & Silver, 1998). The modern utility
 140 of this method is that it allows a wide range of model parameters to be explored within
 141 a timely manner, as discussed in Section 2.3.

142 **2.2 Localization via Slepian Functions**

143 Our regional analyses use Slepian functions to perform a spatio-spectral localiza-
 144 tion of the dynamic geoid kernels and surface datasets such as the geoid, dynamic to-
 145 pography, etc. Slepian functions are well studied in the literature (e.g. Dahlen & Simons,
 146 2008; Harig et al., 2015; Simons et al., 2006; Simons, 2010; Wiczorek & Simons, 2005),
 147 and here we present a brief overview of their construction.

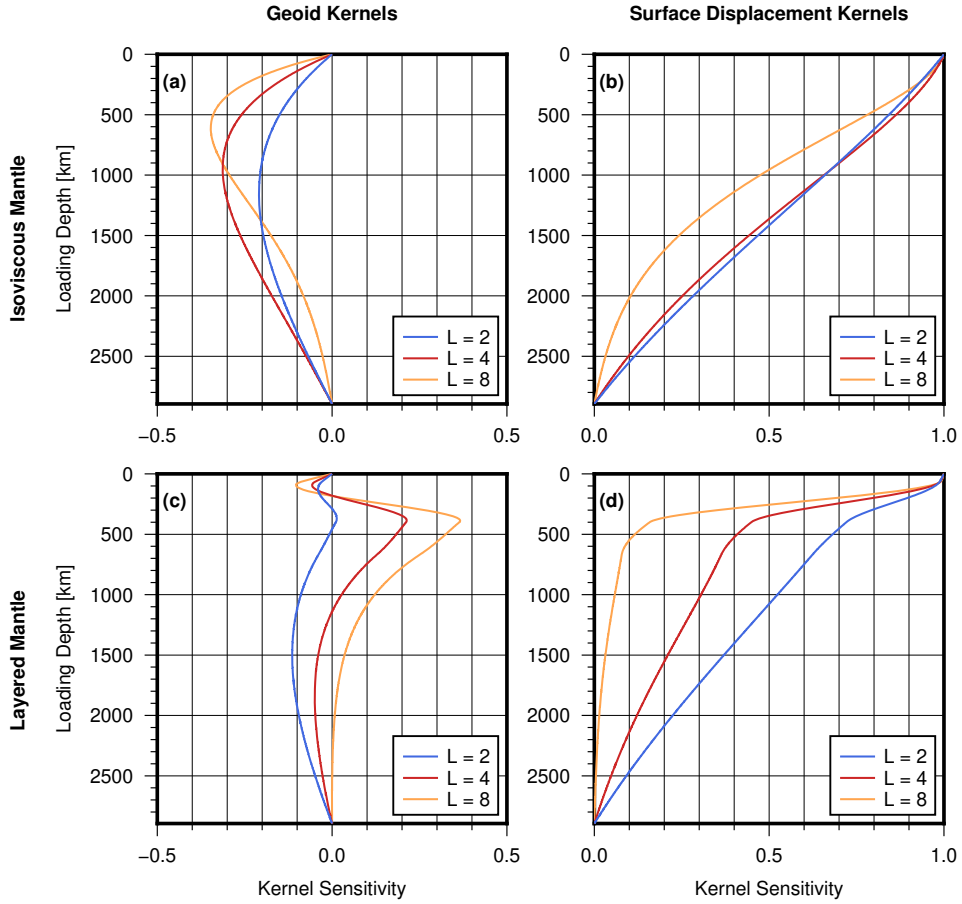


Figure 2. Plots of geoid kernels for (a) an isoviscous mantle and (c) a layered mantle; and the corresponding surface displacement kernels for the same (b) isoviscous mantle and (d) layered mantle. These are plotted as a function of loading depth (synonymous with mantle depth here) and spherical harmonic degree L . The layered case consists of a moderately strong lower mantle, weak mid mantle and asthenosphere, and strong lithosphere. Functions of progressively higher spherical harmonic orders sample shallower within the mantle. Also, complex models of mantle viscosity typically produce complicated weightings of mantle density structures. These plots are reproductions of parts of Figures 9.21 and 9.24 from Hager & Clayton (1989).

148 Spherical harmonic functions, Y , are orthogonal over the whole sphere, Ω . When
 149 considered over a partial sphere region A , however, they are no longer orthogonal, and
 150 their integral products are no longer delta functions, instead forming a matrix with strong
 151 off-diagonal energy,

$$\int_A Y_{lm} Y_{l'm'} d\Omega = D_{lm,l'm'}. \quad (3)$$

152 We use the ‘localization kernel’ matrix \mathbf{D} to generate the new Slepian functions g by solv-
 153 ing the eigenvalue decomposition such that

$$\sum_{l'=0}^L \sum_{m'=-l'}^{l'} D_{lm,l'm'} g_{l'm'} = \lambda g_{lm}. \quad (4)$$

154 The eigenfunctions of \mathbf{D} then form a new basis which is both orthogonal over the region
 155 and over the whole sphere, where the eigenvalues $0 \leq \lambda \leq 1$ describe the portion of
 156 the function’s energy concentrated within the region A . Here, l and m (and l' , m') are
 157 the spherical harmonic degree and order, respectively.

158 We can form a regional basis by truncating the set of functions when eigenvalues
 159 become low. This sparse representation of data allows very good reconstruction prop-
 160 erties within the region and limits influence from phenomena outside of our region of in-
 161 terest (Harig & Simons, 2012). In this study, we operate the dynamic geoid kernels with
 162 Slepian localization functions to create local geoid kernels, which are now localized in
 163 three-dimensional space. Thus, the regional viscosity inversions are based solely on the
 164 structure of the mantle beneath southern Africa.

165 Our study region is defined by the coastal outline of Africa for the southern, east-
 166 ern, and western borders and latitude 1° N for the northern border (see Figure 1(a)).
 167 This region encompasses all areas of high elevation in southern Africa, besides that be-
 168 longing to the northern portion of the east African rift system. The efficiency and spar-
 169 sity of a Slepian representation leads to computational savings and reduces the non-uniqueness
 170 of the inverse problem. To accomplish this localization, we have sacrificed complete iso-
 171 lation of signals in the spectral domain. The basis functions are no longer delta func-
 172 tions in the spectral domain. While our basis has perfect localization in the spectral do-
 173 main up to a bandlimit, each individual function has energy spread over each degree up
 174 to L instead of just a single degree.

2.3 Bayesian Algorithm

We invert for radial viscosity profiles and the corresponding models of dynamic topography by using transdimensional, hierarchical Bayesian inference (Sambridge et al., 2013), specifically a reversible-jump Markov-chain Monte Carlo (MCMC) algorithm (Green, 1995). The algorithm used in this study closely follows the methods outlined by Rudolph et al. (2015). It traverses a complex model space while searching for a global minimum, which we assume is the true model of the Earth’s mantle. At each iteration of the MCMC algorithm, there is an equal probability of five outcomes: creation of a viscosity jump at a random depth, deletion of a viscosity jump at a random depth, moving a random viscosity jump to a new random depth, changing the value of a random jump, or changing the estimate of the variance of the data in the model.

Each run of the MCMC algorithm is initialized with a single relative viscosity jump at a depth of 180 *km*, where the viscosity above this depth is one order of magnitude higher than that below it. This depth is chosen because it is a conservative estimate of where the lithosphere beneath southern Africa terminates, based on inspection of the seismic tomography models used in this study. It is also consistent with geodynamic (Globig et al., 2016) and seismologic studies (Fishwick, 2010; Pasyanos & Nyblade, 2007) of the African lithosphere.

During the first iteration, the geoid is calculated according to the method outlined in Section 2.1. If this is a regional model, the geoid is calculated using local dynamic kernels (Section 2.2). We calculate the misfit (quadratic norm) between the observed and calculated geoid (either globally or regionally). The viscosity structure is then perturbed through one of the five possible steps outlined above, and the geoid and misfit are computed again. This new misfit is then used to determine the likelihood function as

$$P(M|O) = \frac{1}{\sqrt{(2\pi)^n}} \exp\left(-\frac{\phi(O)}{2}\right). \quad (5)$$

Here, n is the number of spherical harmonic functions ($n = (L + 1)^2$); M is the proposed model; and O is the operator that yields the synthetic model of the geoid. $\phi(O) = \mathbf{W}^T \mathbf{I} \mathbf{W}$, which is the Mahalanobis distance, where \mathbf{W} is the model misfit. The probability of acceptance for the new model is then

$$\min\left(1, \frac{P(M|O')}{P(M|O)} \frac{k+1}{k'+1}\right), \quad (6)$$

203 where k is the number of viscosity layers. The primed variables correspond to the pro-
204 posed model, and the unprimed variables correspond to the previous model. This pro-
205 posed model is either accepted or rejected, and the algorithm moves to the next itera-
206 tion, where the above process is repeated for a new perturbation. Equations 5 and 6 are
207 modified from Rudolph et al. (2015), whose implementation of Bayesian techniques and
208 notation follows closely that of Kolb & Lekić (2014).

209 We run each inversion for one million iterations, with the expectation that the model
210 requires such a high number of iterations to converge at a solution. We computed sev-
211 eral inversions for two million iterations as a means to verify that we use enough iter-
212 ations to allow the models to find the global minimum. The ensemble averages of these
213 tests at two million iterations are not significantly different from those at one million it-
214 erations. This gives us confidence that our resulting models of mantle viscosity are both
215 well-constrained by the observed geoid and close to the global minimum of our model
216 space. We compute the resulting ensemble average for a given inversion from the final
217 two hundred thousand iterations. Since the ensemble average is a statistical entity and
218 not physically meaningful, we use the viscosity profile from the final iteration as our so-
219 lution to each inversion. We then pass the final viscosity profile back into the correspond-
220 ing forward model to create updated kernels, which calculate the resulting predicted dy-
221 namic topography.

222 We run both global and regional viscosity inversions over a range of sixteen differ-
223 ent mantle density models. For each analysis, we create a given density model by mul-
224 tiplying an existing shear wave seismic tomography model with a seismic scaling pro-
225 file, $R_{\rho/s} = d[\ln\rho]/d[\ln V_s]$. $R_{\rho/s}$ converts shear wave velocity to density as a function
226 of depth within the mantle. We use four different whole-mantle global tomography mod-
227 els: S40RTS (Ritsema et al., 2011), SEMUCB-WM1 (French & Romanowicz, 2014), SAW642ANb
228 (Panning et al., 2010), and S362WMANI+M (Moulik & Ekström, 2014). We combine
229 these tomography models with four different seismic scaling profiles: the “thermal velocity-
230 density” scaling relationship produced by Simmons et al. (2007) and three depth-constant
231 scaling profiles with values 0.2, 0.3, and 0.4. We choose four distinct seismic tomogra-
232 phy models to examine the effect of the variance between these models on the resulting
233 mantle viscosity profiles and dynamic topography. All four tomography models were cre-
234 ated within the past fifteen years, ensuring reasonable data coverage beneath southern

235 Africa. These are also all global shear-wave velocity models, allowing direct comparison
236 between global and regional inversions.

237 Several regional seismic tomography models exist for southern Africa (e.g. Begg et
238 al., 2009; Emry et al., 2019), but we chose not to use them for our study. These mod-
239 els have improved resolutions of the crust and upper mantle, but contain little to no data
240 below depths of 400 *km*. Although our regional inversions are not heavily influenced by
241 the lower mantle, placing no constraints on depths below 400 *km* would skew our mod-
242 els towards unrealistic results. We instead use four global tomography models with av-
243 erage to above average coverage for the whole mantle beneath southern Africa.

244 Our observed geoid, the primary constraint on our viscosity inversions, is that of
245 EGM2008 (Pavlis et al., 2012) truncated between spherical harmonic degree and order
246 2 and 20. For our regional inversions, both the observed and computed geoid are local-
247 ized to our region for comparison. We set 3200 kg/m^3 as the average density of the man-
248 tle. The mantle tomography models are discretized at a depth interval of 10 *km* to re-
249 solve all structures large enough to be detected at degree 20. We zero out the density
250 contributions from layers shallower than 180 *km* when computing the model geoid. As
251 mentioned above, 180 *km* is a conservative estimate of the depth of the lithosphere be-
252 neath southern Africa. We do not want the lithosphere to contribute to our calculations
253 of dynamic topography. Each inversion is allowed to insert at most 9 viscosity discon-
254 tinuities, or “jumps,” in addition to the initial fixed discontinuity at the base of the litho-
255 sphere. We impose this condition to limit the complexity of our final models.

256 2.4 GNSS Vertical Displacement

257 In addition to our modeling work, we use long-term vertical GNSS timeseries to
258 analyze the vertical displacement in southern Africa. We collect these timeseries from
259 112 stations hosted by the University of Nevada Reno Geodetic Laboratory (Blewitt et
260 al., 2018). These stations lie within the same region as defined for the Bayesian inver-
261 sions. Only stations with data spanning a period of at least 3 years were chosen for our
262 analysis. We use the geodetic program Hector (Bos et al., 2013) to compute the linear
263 vertical displacement rate for each station.

264 We project these rates into a Slepian basis and localize them within our region to
265 form a spatial map, allowing for straightforward comparison with the estimates of dy-

266 namic topography. Our Slepian basis covers the same bandwidth as the Bayesian inver-
267 sions ($2 \leq L \leq 20$), ensuring that all energy in this new basis is representative of only
268 regional motions. By removing higher order spherical harmonics, we also remove station-
269 dependent effects in areas with good station coverage. See Knowles et al. (2020) for a
270 more detailed review of the utility that Slepian localization techniques provide to the es-
271 timation of regional motion with GNSS timeseries.

272 We correct the GNSS linear displacement trends for the effects of glacial isostatic
273 adjustment (GIA), changes in present-day water storage, and trends in atmospheric pres-
274 sure by using data from the Gravity Recovery and Climate Experiment (GRACE) and
275 follow on mission. We use the Center for Space Research (CSR) release level 5 (GRACE)
276 data (Save et al., 2016), adding back the atmosphere and ocean model which is removed
277 by default. We convert water loading into vertical displacement using load Love num-
278 bers (Wahr et al., 1998), in the same manner as Knowles et al. (2020). This product should
279 also contain temporal geopotential trends due to tectonic/dynamic motions, but the mag-
280 nitude would be dwarfed by any signals from the surface water cycle. We compute the
281 corrected linear trend of vertical displacement due to changes in water storage at the GNSS
282 station locations and project these trends into a Slepian basis for our region. The result-
283 ing model contains signal only from long wavelength, regional vertical motions. We per-
284 form this same correction for the GNSS station vertical uncertainties.

285 **3 Results**

286 **3.1 Mantle Viscosity**

287 For each of our 32 Bayesian inversions, we plot the ensemble viscosity interface prob-
288 ability distributions as a function of depth within the mantle. Here we discuss results
289 of the inversions that use S40RTS as the seismic tomography model (Figure 3), while
290 the results for the other tomography models are available in the Supporting Information.
291 These distributions illustrate the depth and viscosity of layers preferentially inserted by
292 the inversion for the final two hundred thousand iterations. The black line represents the
293 ensemble average of the final iterations for each inversion and should not be interpreted
294 as the mantle final viscosity profile.

295 The interface distributions for the global inversions (Figure 3, top row) with con-
296 stant scaling profiles (b)–(d) are consistent between all of the seismic tomography mod-

297 els. These inversions all produce a strong lithosphere, a weak asthenosphere and upper-
298 mantle, a strong mid-mantle, and a weak lower-mantle. The mean ensembles for each
299 of these inversions are all smoothly varying, owing to the wide spread of potential in-
300 version solutions. This is in contrast to the level of complexity seen in each of the global
301 inversions that use the Simmons et al. (2007) scaling profile (e.g. Figure 3(a)). While
302 the exact depth and values of viscosity interfaces vary for each inversion, the overall pat-
303 tern is consistent: strong lithosphere, weak asthenosphere, strong mantle transition zone,
304 weak layer at or below 1000 *km*, strong layer in the upper portion of the lower-mantle,
305 and a very weak lowermost mantle. This same viscosity distribution as a function of depth
306 is not observed in any of the $R_{\rho/S} = \text{constant}$ global inversions, suggesting that the
307 model constraints used to create the Simmons et al. (2007) scaling profile heavily con-
308 trol the output of our corresponding viscosity inversions.

309 The interface distributions for the regional inversions (Figure 3, bottom row) dif-
310 fer substantially from those of the global inversions in their overall pattern, model spread,
311 and complexity. These model solutions tend to favor a strong lithosphere, weak astheno-
312 sphere and mantle transition zone, strong mid- and lower mantle, and weak base of the
313 mantle. The spread of ensemble solutions as a function of viscosity is quite tight (typ-
314 ically less than 0.2 *Pa·s*), except in the top of the lower mantle (specifically, between
315 depths of 1000 and 1700 *km*). At these depths, the regional inversions slightly favor a
316 low viscosity channel, but due to the ensemble spread, a higher viscosity is also some-
317 what likely for this depth range and would be more compatible with the viscosities of
318 the layers immediately above and below. There is also greater consistency between en-
319 semble solutions for the regional inversions as opposed to the global inversions when com-
320 paring the Simmons et al. (2007) scaling profile with the $R_{\rho/S} = \text{constant}$ scaling pro-
321 files.

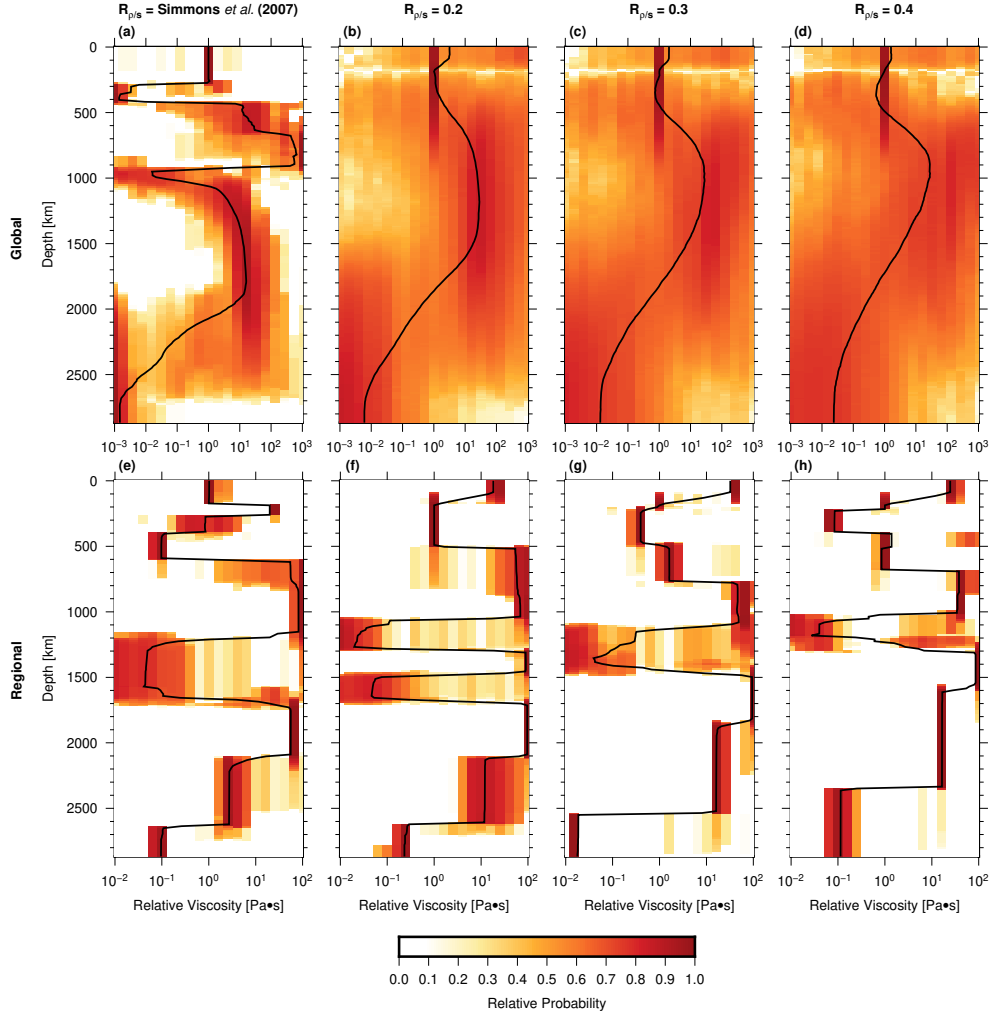


Figure 3. Viscosity inversion ensemble solutions for tomography model S40RTS. The top row (a)–(d) contains the results of the global inversions, while the bottom row (e)–(h) contains the results of the regional inversions. Each column contains the results for a different scaling profile; from left to right: (a),(e) Simmons et al. (2007); (b),(f) 0.2; (c),(g) 0.3; and (d),(h) 0.4. The black line in each plot is the ensemble average viscosity profile for the final two hundred thousand iterations of the inversion. The color gradient represents the normalized probability for the insertion of an interface at a specific depth and viscosity value.

322

3.2 Dynamic Topography

323

The synthetic surface dynamic topography computed from the final iteration of each Bayesian inversion is displayed in the same arrangement as the viscosity ensemble re-

324

325 sults, with global results in the top row and regional results in the bottom row. We show
326 results utilizing S40RTS here (Figure 4) with the dynamic topography solutions for ad-
327 ditional tomographic model results in the Supporting Information. In the global cases,
328 dynamic topography is calculated globally and then localized using Slepian functions to
329 our region for ease of comparison with the regional inversions.

330 The range of amplitudes for each plot of dynamic topography exhibits significant
331 variance. In general, the amplitude of dynamic topography increases from left (Simmons
332 et al. (2007) scaling) to right ($R_{\rho/S} = 0.4$) in each figure due to the general increase
333 in density (and thus buoyancy force). For example, the regional $R_{\rho/S} =$ Simmons et
334 al. (2007) solution has a maximum amplitude below 500 m , while the regional $R_{\rho/S} =$
335 0.4 solution has a maximum amplitude that exceeds 3000 m . When comparing the so-
336 lutions from different seismic tomography models with the same scaling profile, the am-
337 plitudes are consistent. Similarly, the pattern of dynamic topography is consistent among
338 the results from each seismic tomography model. Overall, the input seismic tomogra-
339 phy model is the primary control on the pattern of surface dynamic topography, while
340 the scaling profile is the primary control on the amplitudes.

341 The amplitudes of dynamic topography for the regional inversions are greater than
342 the amplitudes for each corresponding global inversion. In most cases, the amplitudes
343 are modest, ranging from 200 to 1000 m . Several inversions produce amplitudes greater
344 than 2000 m , most notably the regional models using the $R_{\rho/S} = 0.3$ and 0.4 scaling
345 profiles. Another consistent feature between the models of dynamic topography is the
346 presence of three lobes (Figure 4(a)-(h)): one in the south (centered over Botswana), one
347 in the northwest (centered over Angola), and one in the northeast (centered over Tan-
348 zania). In each model solution, all three lobes have amplitudes 200–300 m higher than
349 the amplitude of the rest of our region. Outside of the three lobes, predicted dynamic
350 topography is fairly uniform. These three lobes are also present in the models based on
351 the three other seismic tomography models (Figures S4–S6), although the southern lobe
352 dominates the other two lobes in these solutions.

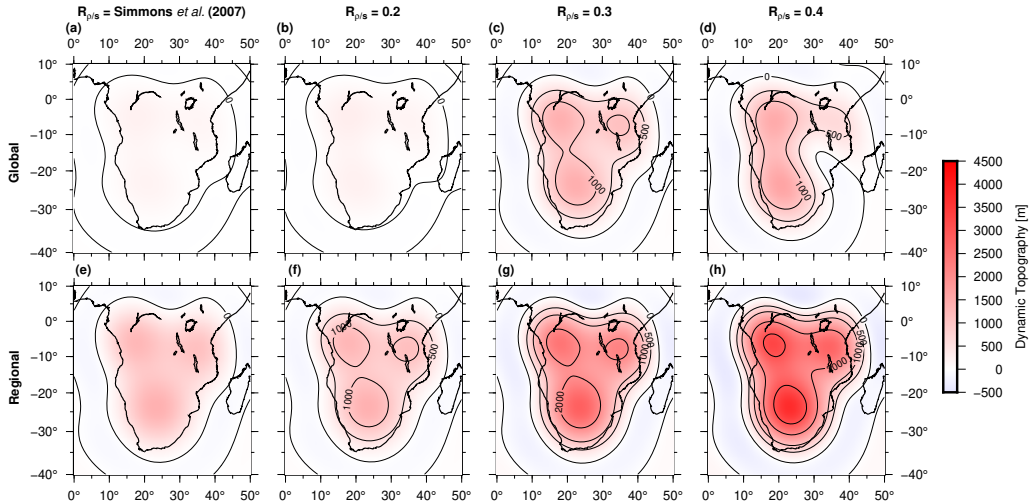


Figure 4. Predicted dynamic topography for tomography model S40RTS. The top row (a)–(d) contains the results of the global inversions, while the bottom row (e)–(h) contains the results of the regional inversions. Each column contains the results for a different scaling profile; from left to right: (a),(e) Simmons et al. (2007); (b),(f) 0.2; (c),(g) 0.3; and (d),(h) 0.4. The dynamic topography is shaded and contoured (at 500, 1000, 2000, 3000, and 4000 m) based on amplitude. All plots have been localized in the southern Africa region defined for this study for ease of comparison.

3.3 Vertical GNSS Motions

The localized, corrected GNSS vertical motions are displayed in Figure 5, and the corresponding uncertainties are displayed in Figure S7. The filled circles represent the individual station motions, while the color gradient represents the motions localized into our regional Slepian basis. Regional uncertainty generally scales inversely with station density. Regional motions are therefore well determined south of a latitude of roughly 20°S , based on the overall uncertainty within this sub-region. The amplitude of the GRACE correction is low relative to that of the uncorrected signal – up to 0.7 mm/yr – with most of the study area exhibiting an overall correction less than 0.2 mm/yr .

Across southern Africa we see mostly broad, low magnitude, and positive vertical motions (Figure 5). The magnitude of these motions is $1\text{--}2\text{ mm/yr}$ in most of the region, with the area in the northwest part of our region (centered over Angola) exceeding 6 mm/yr . There is also a small north central sub-region (centered over the Democratic Republic

366 of the Congo) which exhibits low amplitude negative vertical motions. This particular
 367 pattern is driven by four proximal stations with negative velocities. The pattern of ver-
 368 tical motions is somewhat similar to the pattern of dynamic topography resulting from
 369 several of the models in Section 3.2. There are three primary lobes of positive motion
 370 in the south, northwest, and northeast parts of our region, although the amplitude of
 371 the southern lobe is more subdued than those of the northern lobes. Our confidence in
 372 the two positive northern lobes, especially the northwest lobe, is low due to the poor sta-
 373 tion density and high uncertainty of the signal from these few stations in both sub-regions.

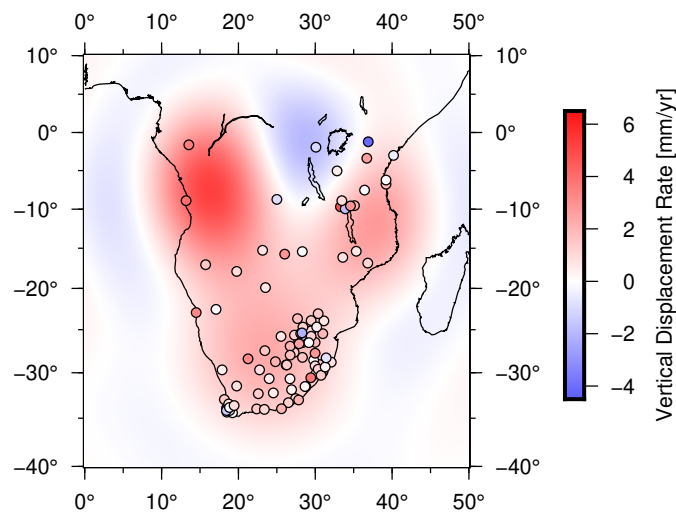


Figure 5. Long-term vertical rates from GNSS within our study region. Individual station motions are plotted as filled circles. The localized regional motion is plotted as a color gradient. Areas in the northern part of our region have the highest velocity amplitudes as well as the highest uncertainties due to the poor station coverage in these areas. The corresponding map of uncertainty can be found in the Supporting Information (Figure S7).

374 4 Discussion

375 4.1 Constraints on mantle viscosity structure

376 In comparing the results of our regional viscosity inversions, it is clear that the choice
 377 of seismic tomography model has a strong effect. Our regional inversions that use S40RTS
 378 (Ritsema et al., 2011) as the input seismic tomography model (Figure 3,(e)–(h)) produce

379 fewer jumps that alternate between low and high viscosity than the regional inversions
380 that use the other three seismic tomography models in this study (Figures S1–S3,(e)–
381 (h)). This alternating viscosity pattern is especially favored by the regional inversions
382 which use S362WMANI+M (Figure S3(e)–(h)), likely owing to the whole-mantle anisotropic
383 nature of that model (Moulik & Ekström, 2014). Such alternations in viscosity confined
384 to thin (approx. 200 km thick) layers are not compatible with our knowledge of heat dif-
385 fusion in Earth’s mantle (Bercovici et al., 2000).

386 Following the above reasoning, we favor the regional inversions that use S40RTS,
387 as the resulting viscosity profiles contain smoother, more physically feasible depth vari-
388 ation. The results of these four regional inversions all contain one or more low viscos-
389 ity channels between 1000 and 1700 km depth. Only the inversions that use the $R_{\rho/S}$ = Simmons
390 et al. (2007) (Figure 3(e)) and the $R_{\rho/S} = 0.3$ (Figure 3(g)) scaling profiles produce
391 mid-mantle low viscosity channels that are more than several hundred kilometers thick.
392 Additionally, the $R_{\rho/S}$ = Simmons et al. (2007) inversion does not produce a strong
393 lithosphere, unlike the other three scaling profiles. For these reasons, we select the $R_{\rho/S}$ =
394 0.3 with S40RTS regional inversion as our preferred model of mantle viscosity beneath
395 southern Africa.

396 Our preferred model of radial viscosity is similar to the results of both Mitrovica
397 & Forte (2004) and Rudolph et al. (2020), who both perform inversions for global ra-
398 dial mantle viscosity. They both see the same viscosity jump just below the mantle tran-
399 sition zone and a low viscosity channel in the mid-mantle. Unique to our model, though,
400 is the presence of a low viscosity channel in the middle of the mantle, between depths
401 of 1100 and 1500 km. It is important to note, however, that although the ensemble av-
402 erage favors a low viscosity at these depths, a significant proportion of the ensemble mod-
403 els favor much higher viscosities which then don’t produce this low viscosity channel. Over-
404 all, our inversion produces a wide range of potential viscosities for this zone of depths
405 in the middle of the mantle.

406 We compute global inversions to compare with the regional models to judge the
407 utility of regional inversions. The results of our global inversions all have wide uncer-
408 tainty across the entire depth-range of the mantle (Figure 3). This is exemplified by both
409 the viscosity spreads and smoothness of the ensemble averages for each of these inver-
410 sion results, especially in the $R_{\rho/S} = \text{constant}$ cases. In other words, there are not enough

411 constraints from the global geoid alone to allow for the estimation of radial mantle vis-
412 cosity. Additionally, given the general complexity of mantle deformation and rheology
413 (e.g. Jackson & Faul, 2010; Yang & Gurnis, 2016), this type of radial profile is likely not
414 applicable to our study region, as a global inversion incorporates mantle dynamic pro-
415 cesses not present in southern Africa (e.g. subduction zones and mid-ocean ridges). It
416 is likely that a global average viscosity profile is not representative of any one particu-
417 lar region, so using such a profile to produce geodynamic models in our study region is,
418 therefore, problematic, and caution is warranted for regional studies.

419 The regional Bayesian inversions allow our analyses to examine effective lateral vari-
420 ations in viscosity within the Earth’s mantle by solving for radial viscosity profiles in dif-
421 ferent regions. The localization of the geoid kernels ensures the regional inversions are
422 influenced only by the structure of the mantle beneath southern Africa. The localiza-
423 tion process itself is flexible and can be easily applied in different regions. One caveat
424 is that the region must not be too small for the given bandwidth L considered. In this
425 case, the Slepian basis would contain too few functions with acceptable eigenvalues (Si-
426 mons et al., 2006). The same issue essentially applies in the depth dimension for differ-
427 ent reasons. As depth within the mantle increases, the contributions to the surface grav-
428 ity field can only be determined at long-wavelengths, which are inherently less well lo-
429 calized (Hager et al., 1985; Hager & Clayton, 1989). If the region of interest is small, the
430 resulting geoid field will not contain much energy from lower mantle processes. The Bayesian
431 inversion for viscosity will then be imprecise at greater depths, as it will try to constrain
432 physical parameters for which it has little to no data.

433 Our inversions incorporate several assumptions about the structure of the mantle
434 and lithosphere. In the global inversions, the relative viscosity profile is allowed to vary
435 by six orders of magnitude of variation, which is a very liberal estimate of the range of
436 mantle viscosity (Flament et al., 2013). We expect that this will encompass all possi-
437 ble values of viscosity within the mantle. For regional inversions, the relative viscosity
438 profile is allowed to vary by only four orders of magnitude. This narrower range lowers
439 the number of iterations necessary for our inversion to converge upon a final solution.
440 We do not believe that the narrower range will bias the regional inversions toward in-
441 serting more viscosity jumps to account for the smaller magnitude of these interfaces,
442 depending on the overall smoothness of the input density model. In fact, it seems likely

443 that viscosity will not vary greatly, since there is likely little lateral variation in viscos-
444 ity within a given region of interest (Yang & Gurnis, 2016).

445 We explore several different shear-wave velocity to mantle density scaling profiles,
446 including those that are constant ($R_{\rho/S} = 0.2, 0.3, \text{ and } 0.4$) and heterogeneous ($R_{\rho/S} =$ Simmons
447 et al. (2007)), to examine their impact on the inversion results. The constant scaling pro-
448 files assume a purely thermal contribution to seismic velocity heterogeneity throughout
449 the mantle, which is not supported by recent seismic and geodynamic studies (Lau et
450 al., 2017; Moulik & Ekström, 2014; F. D. Richards et al., 2023; Ritsema & Lekić, 2020).
451 We include the Simmons et al. (2007) scaling profile, as it was specifically created to rep-
452 resent the thermochemical heterogeneities present in our study region. Without better
453 constraints from mineral physics and seismology on compositional heterogeneity (Sim-
454 mons et al., 2009), especially within the African LLSVP, our choice of scaling profiles
455 attempts to broadly cover the model space. Despite the differences between each of the
456 individual scaling profiles, the regional inversion results for any given seismic tomogra-
457 phy model show strong similarities. The only major exception is in the middle of the man-
458 tle, which has the poorest coverage in our region for all of the seismic tomography mod-
459 els we use.

460 Our preferred viscosity model suggests that there is internal layering within the African
461 LLSVP, with a strong top 600 *km* and very weak bottom 400 *km*, assuming a 1000 *km*
462 total thickness (Lekić et al., 2012). This result is similar to other geodynamic studies
463 who argue for internal layering within LLSVPs consisting of a dense base overlain by a
464 much lighter layer (Liu & Zhong, 2015; F. D. Richards et al., 2023). This same vertical
465 heterogeneity appears in our results, but the viscosity of each layer should not be over-
466 interpreted, as it is a function of the assumed density model.

467 **4.2 Dynamic topography**

468 Our preferred model (Figure 4(g)) produces dynamic topography around 1000 *m*
469 across most of the region with three lobes (south, northeast, and northwest) that extend
470 just beyond 2000 *m*. These three sub-regions are also roughly where the highest topog-
471 raphy currently exists (Figure 1(a)). Our model predicts higher amplitudes of dynamic
472 topography than back-of-the-envelope studies, which predict dynamic topography to be
473 on the order of 200 *m* (e.g. Molnar et al., 2015). Our results are also modest compared

474 to several instantaneous and time-integrated models, which claim dynamic topography
475 in southern Africa exceeds 2000 m (e.g. Forte et al., 1993; Steinberger et al., 2017). Nonethe-
476 less, the $R_{\rho/S}$ = Simmons et al. (2007) scaling profile predicts at least 400 m of dy-
477 namic topography, which is more than double the maximum estimate from Molnar et
478 al. (2015). Based on the range of dynamic topography in our preferred model and the
479 amount of present-day topography, we argue that the southern African lithosphere is al-
480 most entirely dynamically supported by the mantle. Given that our estimate of dynamic
481 topography exceeds the present-day topography in some sub-regions, particularly the north
482 central part of our region, there must be significant erosional forces competing with the
483 upward mantle motion (Moucha & Forte, 2011).

484 It is important to note some of the same caveats about our choice of shear wave
485 velocity to density scaling profiles as in Section 4.1. When comparing our results, the
486 estimated dynamic topography is a strong function of scaling profile, with even a small
487 increase from $R_{\rho/S} = 0.2$ to 0.3 doubling the overall amplitude (Figure 4(f),(g)). Based
488 on these results, even with a well-constrained viscosity profile for a specific region, there
489 needs to be some degree of knowledge about the thermochemical properties of the man-
490 tle to accurately predict dynamic topography. We expect that both the viscosity and the
491 seismic wave speed to density scaling profile change as a function of location within the
492 mantle (e.g. F. D. Richards et al., 2023; Yang & Gurnis, 2016). Future work should in-
493 vestigate placing tighter constraints on the regional scaling profile based on seismic and
494 geodynamic inferences, as suggested by Rudolph et al. (2020).

495 All of our inversions are constrained by the geoid using spherical harmonic degrees
496 2–20. Previous geodynamic studies of dynamic topography use a much narrower range
497 of geoid data, with most extending out to degree and order 8 or 10 (e.g. Hager et al., 1985;
498 Flament et al., 2013; Molnar et al., 2015). We contend that a wider bandwidth is nec-
499 essary to better characterize the magnitude and spatial pattern of dynamic topography.
500 As suggested by Davies et al. (2019), the global spectra of residual topography contains
501 significant power out to degree and order 30, yet most instantaneous-flow simulations
502 have power out to only degree and order 5. We do not extend our analyses beyond de-
503 gree and order 20, because crustal effects dominate at higher orders (Hoggard et al., 2016).
504 Additionally, the global tomography models used in this study contain minimal power
505 above degree and order 20, preventing us from constraining models at these higher or-
506 ders.

507 This technique of computing regional viscosity profiles will prove useful in other
508 regions where there is contention over the amplitude of dynamic topography. The region
509 surrounding the New Hebrides Trench near Vanuatu and New Caledonia appears to be
510 experiencing uplift related to slab detachment (Chatelain et al., 1992). Meanwhile, the
511 Brazilian Highlands are at a relatively high elevation - on the order of 2000 *m* - yet are
512 not near any major surface tectonic features (Flament et al., 2014). Dynamic topogra-
513 phy has been attributed to both regions, yet estimates of the amplitudes are not in good
514 agreement. The methods presented in this paper could elucidate the magnitude of the
515 mantle dynamic processes that control these features.

516 4.3 Vertical displacement

517 Three lobes of positive vertical motion are displayed in the GNSS vertical motions
518 (Figure 5), all of which correlate with the three lobes of dynamic topography in the south,
519 northwest, and northeast parts of our region. The southern lobe is well-constrained by
520 a dense station network, indicating that the roughly 1 *mm/yr* of vertical motion there
521 is a real feature. The other two lobes don't have the same station coverage, which is re-
522 flected in the high uncertainty in these sub-regions. The northwest lobe is in the same
523 sub-region as the Bié Plateau which, as determined by Walford & White (2005), has ex-
524 perience uplift over the last 30 *Myr*, as evidenced by erosional unconformities in seis-
525 mic reflection data. It is likely that at least a portion of the vertical motion recorded by
526 GNSS stations in these regions is due to regional uplift; however, it is not as high as in-
527 dicated by the results of our analysis. More station coverage and longer baselines are nec-
528 essary to better constrain the amplitude of these features.

529 The vertical GNSS velocities computed in this study are similar to those estimated
530 by both Hammond et al. (2021) and Saria et al. (2013). This gives us confidence that
531 most of the stations used in this study have long enough baselines to reflect ongoing dy-
532 namic topography changes, as the rates are consistent through several decades of record-
533 ing. In particular, Hammond et al. (2021) note that the long wavelength, coherent ver-
534 tical displacement in southern Africa likely reflects a mantle geodynamic source. Based
535 on these results, it is reasonable to conclude that up to 1.5 *mm/yr* of uplift is occurring
536 in southern Africa. Given that most of our region is at an elevation above 1.5 *km*, and
537 assuming an initial elevation at sea level, then this uplift could have occurred within the
538 past 1 *Myr*. This does not account for denudation or variations in the uplift rate through

539 time, both of which are non-negligible (Moucha & Forte, 2011; Walford & White, 2005).
540 While the exact initiation of the uplift of the Southern African Plateau cannot currently
541 be constrained (Artyushkov & Hofmann, 1998; Jones et al., 2017), these results suggest
542 that uplift has occurred recently and is ongoing.

543 **5 Conclusions**

544 We computed both global and regional inversions for the mantle’s radial viscosity
545 profile as constrained by the non-hydrostatic geoid. Based on the regional inversions, we
546 can conclude that (1) the viscosity profile beneath southern Africa has a strong litho-
547 sphere, a weak asthenosphere and mantle transition zone, a strong mid-mantle punctu-
548 ated by a low viscosity channel, and a very weak mantle base; and (2) there is internal
549 layering in the African LLSVP, which has a strong upper portion underlain by a much
550 weaker base. By comparing the regional and global inversions, we notice that lateral vis-
551 cosity variations are an important consideration, as regional differences in viscosity are
552 significant. Our resulting computation of dynamic topography based on the regional in-
553 versions allows us to determine that the magnitude of dynamic topography in southern
554 Africa ranges from 1000 to 2000 m , with a minimum value near 500 m . Our localization
555 technique for vertical GNSS station motion in southern Africa also indicates that there
556 exists long-wavelength vertical displacement of up to 1.5 mm/yr throughout most of the
557 region. In summary, a moderate amount of dynamic topography is shown to exist in south-
558 ern Africa, the formation of which is an ongoing process and spans at least the past sev-
559 eral million years.

560 **Open Research Section**

561 The code used in this work is available freely online (Harig et al., 2015) as part of
562 the SLEPIAN code package, specifically *Slepian Tango* ([https://github.com/csdms-
563 -contrib/slepian_tango](https://github.com/csdms-contrib/slepian_tango)). Installation instructions for the various Slepian code repos-
564 itories can be found at <http://github.com/Slepian/Slepian>.

565 **Acknowledgments**

566 This work was supported by the National Science Foundation (NSF) via grant NSF-2142980
567 funded by the Geophysics program, and by the National Aeronautics and Space Admin-
568 istration (NASA) via grant NNX17AE18G funded by the Interior of the Earth program,

569 both to C.H. Figures were plotted using the Generic Mapping Tools (Wessel et al., 2013).
570 We would like to thank Dr. Anthony Osei Tutu for his contributions to the development
571 of the software and Dr. Kiriaki Xiluri-Lauria for her tireless technical support.

572 **References**

- 573 Al-Hajri, Y., White, N. J., & Fishwick, S. (2009). Scales of transient convective sup-
574 port beneath Africa. *Geology*, *37*(10), 883–886. doi: 10.1130/G25703A.1
- 575 Amante, C., & Eakins, B. W. (2009). ETOPO1 1 Arc-Minute Global Relief Model:
576 Procedures, Data Sources and Analysis. *NOAA Technical Memorandum NESDIS*
577 *NGDC-24*. National Geophysical Data Center, NOAA. doi: 10.7289/V5C8276M
- 578 Artyushkov, E. V., & Hofmann, A. W. (1998). Neotectonic Crustal Uplift on the
579 Continents and its Possible Mechanisms. The Case of Southern Africa. *Surveys in*
580 *Geophysics*, *19*(5), 369–415. doi: 10.1023/A:1006563824961
- 581 Begg, G. C., Griffin, W. L., Natapov, L. M., O’Reilly, S. Y., Grand, S. P., O’Neill,
582 C. J., . . . Bowden, P. (2009). The lithospheric architecture of Africa: Seismic to-
583 mography, mantle petrology, and tectonic evolution. *Earth and Planetary Science*
584 *Letters*, *5*(1), 23–50. doi: 10.1130/GES00179.1
- 585 Bercovici, D., Ricard, Y., & Richards, M. A. (2000). The relation between man-
586 tle dynamics and plate tectonics: A primer. In *The history and dynamics of global*
587 *plate motions* (p. 5-46). American Geophysical Union (AGU). doi: [https://doi](https://doi.org/10.1029/GM121p0005)
588 [.org/10.1029/GM121p0005](https://doi.org/10.1029/GM121p0005)
- 589 Blewitt, G., Hammond, W. C., & Kreemer, C. (2018). Harnessing the GPS data ex-
590 plosion for interdisciplinary science. *Eos*, *99*. doi: 10.1029/2018EO104623
- 591 Bos, M. S., Fernandes, R. M. S., Williams, S. D. P., & Bastos, L. (2013). Fast Er-
592 ror Analysis of Continuous GNSS Observations with Missing Data. *Journal of*
593 *Geodesy*, *87*(4), 351–360. doi: 10.1007/s00190-012-0605-0
- 594 Chatelain, J.-L., Molnar, P., Prévot, R., & Isacks, B. (1992). Detachment of part of
595 the downgoing slab and uplift of the New Hebrides (Vanuatu) Islands. *Geophysical*
596 *Research Letters*, *19*(14), 1507–1510. doi: 10.1029/92GL01389
- 597 Colli, L., Ghelichkhan, S., & Bunge, H.-P. (2016). On the ratio of dynamic topog-
598 raphy and gravity anomalies in a dynamic Earth. *Wiley-Blackwell*, *43*(6), 2510–
599 2516. doi: 10.1002/2016GL067929
- 600 Dahlen, F. A., & Simons, F. J. (2008). Spectral estimation on a sphere in geophysics

601 and cosmology. *Geophys. J. Int.*, *174*, 774–807. doi: 10.1111/j.1365-246X.2008
602 .03854.x

603 Davies, D. R., Valentine, A. P., Kramer, S. C., Rawlinson, N., Hoggard, M. J.,
604 Eakin, C. M., & Wilson, C. R. (2019). Earth’s multi-scale topographic response to
605 global mantle flow. *Nature Geoscience*. doi: 10.1038/s41561-019-0441-4

606 de Wit, M. (2007). The Kalahari Epeirogeny and climate change: differentiating
607 cause and effect from core to space. *South African Journal of Geology*, *110*(2-3),
608 367-392. doi: 10.2113/gssajg.110.2-3.367

609 Emry, E. L., Shen, Y., Nyblade, A. A., Flinders, A., & Bao, X. (2019). Upper man-
610 tle Earth structure in Africa from full-wave ambient noise tomography. *Geochem-*
611 *istry, Geophysics, Geosystems*, *20*, 120–147. doi: 10.1029/2018GC007804

612 Fishwick, S. (2010). Surface wave tomography: Imaging of the litho-
613 sphere–asthenosphere boundary beneath central and southern Africa? *Litho-*
614 *sphere*, *120*(1-2), 63–73. doi: 10.1016/J.LITHOS.2010.05.011

615 Flament, N., Gurnis, M., & Müller, D. (2013). A review of observations and models
616 of dynamic topography. *Lithosphere*, *5*(2), 189–210. doi: 10.1130/L245.1

617 Flament, N., Gurnis, M., Williams, S., Seton, M., Skogseid, J., Heine, C., & Dietmar
618 Müller, R. (2014). Topographic asymmetry of the South Atlantic from global
619 models of mantle flow and lithospheric stretching. *Earth and Planetary Science*
620 *Letters*, *387*, 107–119. doi: 10.1016/J.EPSL.2013.11.017

621 Forte, A. M., Peltier, W. R., Dziewonski, A. M., & Woodward, R. L. (1993). Dy-
622 namic surface topography: A new interpretation based upon mantle flow models
623 derived from seismic tomography. *Geophysical Research Letters*, *20*(3), 225–228.
624 doi: 10.1029/93GL00249

625 Forte, A. M., Quéré, S., Moucha, R., Simmons, N. A., Grand, S. P., Mitrovica, J. X.,
626 & Rowley, D. B. (2010). Joint seismic–geodynamic–mineral physical modelling
627 of African geodynamics: A reconciliation of deep-mantle convection with surface
628 geophysical constraints. *Earth and Planetary Science Letters*, *295*(3-4), 329–341.
629 doi: 10.1016/J.EPSL.2010.03.017

630 French, S. W., & Romanowicz, B. A. (2014). Whole-mantle radially anisotropic
631 shear velocity structure from spectral-element waveform tomography. *Geophysical*
632 *Journal International*, *199*(3), 1303–1327. doi: 10.1093/gji/ggu334

633 Globig, J., Fernández, M., Torne, M., Vergés, J., Robert, A., & Faccenna, C. (2016).

- 634 New insights into the crust and lithospheric mantle structure of Africa from eleva-
635 tion, geoid, and thermal analysis. *Journal of Geophysical Research: Solid Earth*,
636 *121*(7), 5389-5424. doi: 10.1002/2016JB012972
- 637 Green, P. J. (1995). Reversible jump Markov chain Monte Carlo computation and
638 Bayesian model determination. *Biometrika*, *82*(4), 711-732. doi: 10.1093/biomet/
639 82.4.711
- 640 Gurnis, M., Mitrovica, J. X., Ritsema, J., & van Heijst, H.-J. (2000). Constraining
641 mantle density structure using geological evidence of surface uplift rates: The case
642 of the African Superplume. *Geochemistry, Geophysics, Geosystems*, *1*(7). doi:
643 10.1029/1999GC000035
- 644 Hager, B. H., & Clayton, R. W. (1989). Constraints on the Structure of Man-
645 tle Convection Using Seismic Observations, Flow Models, and the Geoid. In
646 W. R. Peltier (Ed.), *Mantle convection: Plate tectonics and global dynamics* (pp.
647 657-763).
- 648 Hager, B. H., Clayton, R. W., Richards, M. A., Comer, R. P., & Dziewonski, A. M.
649 (1985). Lower mantle heterogeneity, dynamic topography and the geoid. *Nature*,
650 *313*(6003), 541-545. doi: 10.1038/313541a0
- 651 Hammond, W. C., Blewitt, G., Kreemer, C., & Nerem, R. S. (2021). Gps imaging of
652 global vertical land motion for studies of sea level rise. *Journal of Geophysical Re-*
653 *search: Solid Earth*, *126*(7), e2021JB022355. doi: 10.1029/2021JB022355
- 654 Harig, C., Lewis, K. W., Plattner, A., & Simons, F. J. (2015). A suite of software
655 analyzes data on the sphere. *Eos*, *96*. doi: 10.1029/2015EO025851
- 656 Harig, C., & Simons, F. J. (2012). Mapping Greenland's mass loss in space and
657 time. *Proceedings of the National Academy of Sciences*, *109*(49), 19934-19937.
658 doi: 10.1073/pnas.1206785109
- 659 Hoggard, M. J., White, N. J., & Al-Attar, D. (2016). Global dynamic topography
660 observations reveal limited influence of large-scale mantle flow. *Nature Geoscience*,
661 *9*(6), 456-463. doi: 10.1038/ngeo2709
- 662 Holdt, M. C., White, N. J., Stephenson, S. N., & Conway-Jones, B. W. (2022).
663 Densely sampled global dynamic topographic observations and their significance.
664 *Journal of Geophysical Research: Solid Earth*, *127*(7), e2022JB024391. doi:
665 10.1029/2022JB024391
- 666 Jackson, I., & Faul, U. H. (2010). Grainsize-sensitive viscoelastic relaxation in

- 667 olivine: Towards a robust laboratory-based model for seismological application.
668 *Phys. Earth Planet. Inter.*, 183, 151-163. doi: 10.1016/j.pepi.2010.09.005
- 669 Jones, A. G., Afonso, J. C., & Fullea, J. (2017). Geochemical and geophysical
670 constrains on the dynamic topography of the Southern African Plateau. *Geochem-*
671 *istry, Geophysics, Geosystems*, 18(10), 3556–3575. doi: 10.1002/2017GC006908
- 672 Knowles, L., Bennett, R. A., & Harig, C. (2020). Vertical displacements of the Ama-
673 zon basin from GRACE and GPS. *Journal of Geophysical Research: Solid Earth*,
674 125(2). doi: 10.1029/2019JB018105
- 675 Kolb, J. M., & Lekić, V. (2014). Receiver function deconvolution using transdimen-
676 sional hierarchical Bayesian inference. *Geophysical Journal International*, 197(3),
677 1719-1735. doi: 10.1093/gji/ggu079
- 678 Lau, H. C., Mitrovica, J. X., Davis, J. L., Tromp, J., Yang, H. Y., & Al-Attar, D.
679 (2017). Tidal tomography constrains Earth’s deep-mantle buoyancy. *Nature*,
680 551(7680), 321–326. doi: 10.1038/nature24452
- 681 Le Stunff, Y., & Ricard, Y. (1997). Partial advection of equidensity surfaces: A solu-
682 tion for the dynamic topography problem? *Journal of Geophysical Research: Solid*
683 *Earth*, 102(B11), 24655–24667. doi: 10.1029/97JB02346
- 684 Lekić, V., Cottaar, S., Dziewonski, A., & Romanowicz, B. (2012). Cluster analysis
685 of global lower mantle tomography: A new class of structure and implications for
686 chemical heterogeneity. *Earth and Planetary Science Letters*, 357-358, 68-77. doi:
687 10.1016/j.epsl.2012.09.014
- 688 Lithgow-Bertelloni, C., & Silver, P. G. (1998). Dynamic topography, plate driv-
689 ing forces and the African superswell. *Nature*, 395(6699), 269–272. doi: 10.1038/
690 26212
- 691 Liu, X., & Zhong, S. (2015). The long-wavelength geoid from three-dimensional
692 spherical models of thermal and thermochemical mantle convection. *Jour-*
693 *nal of Geophysical Research: Solid Earth*, 120(6), 4572-4596. doi: 10.1002/
694 2015JB012016
- 695 Mitrovica, J. X., & Forte, A. M. (2004). A new inference of mantle viscosity based
696 upon joint inversion of convection and glacial isostatic adjustment data. *Earth and*
697 *Planetary Science Letters*, 225(1-2), 177–189. doi: 10.1016/J.EPSL.2004.06.005
- 698 Molnar, P., England, P. C., & Jones, C. H. (2015). Mantle dynamics, isostasy, and
699 the support of high terrain. *Journal of Geophysical Research: Solid Earth*, 120(3),

700 1932–1957. doi: 10.1002/2014JB011724

701 Morgan, W. J. (1965a). Gravity anomalies and convection currents: 1. A sphere and
702 cylinder sinking beneath the surface of a viscous fluid. *Journal of Geophysical Re-*
703 *search*, 70(24), 6175–6187. doi: 10.1029/JZ070i024p06175

704 Morgan, W. J. (1965b). Gravity anomalies and convection currents: 2. The Puerto
705 Rico Trench and the Mid-Atlantic Rise. *Wiley-Blackwell*, 70(24), 6189–6204. doi:
706 10.1029/JZ070i024p06189

707 Moucha, R., & Forte, A. M. (2011). Changes in African topography driven by man-
708 tle convection. *Nature Geoscience*, 4(10), 707–712. doi: 10.1038/ngeo1235

709 Moulik, P., & Ekström, G. (2014). An anisotropic shear velocity model of
710 the Earth’s mantle using normal modes, body waves, surface waves and long-
711 period waveforms. *Geophysical Journal International*, 199(3), 1713–1738. doi:
712 10.1093/gji/ggu356

713 Panning, M. P., Lekić, V., & Romanowicz, B. A. (2010). Importance of crustal
714 corrections in the development of a new global model of radial anisotropy. *Jour-*
715 *nal of Geophysical Research: Solid Earth*, 115(B12), B12325. doi: 10.1029/
716 2010JB007520

717 Pasyanos, M. E., & Nyblade, A. A. (2007). A top to bottom lithospheric study of
718 Africa and Arabia. *Tectonophysics*, 444(1-4), 27–44. doi: 10.1016/J.TECTO.2007
719 .07.008

720 Pavlis, N. K., Holmes, S. A., Kenyon, S. C., & Factor, J. K. (2012). The develop-
721 ment and evaluation of the Earth Gravitational Model 2008 (EGM2008). *Journal*
722 *of Geophysical Research: Solid Earth*, 117(B04406). doi: 10.1029/2011JB008916

723 Ricard, Y., Fleitout, L., & Froidevaux, C. (1984). Geoid heights and lithospheric
724 stresses for a dynamical earth. *Ann. Geophys.*, 2, 267-286.

725 Richards, F. D., Hoggard, M. J., Ghelichkhan, S., Koelemeijer, P., & Lau, H. C.
726 (2023). Geodynamic, geodetic, and seismic constraints favour deflated and
727 dense-cored llvps. *Earth and Planetary Science Letters*, 602, 117964. doi:
728 10.1016/j.epsl.2022.117964

729 Richards, M. A., & Hager, B. H. (1984). Geoid anomalies in a dynamic Earth. *Jour-*
730 *nal of Geophysical Research*, 89, 5987–6002. doi: 10.1029/JB089iB07p05987

731 Ritsema, J., Deuss, A., van Heijst, H.-J., & Woodhouse, J. H. (2011). S40RTS:
732 a degree-40 shear-velocity model for the mantle from new Rayleigh wave

733 dispersion, teleseismic traveltimes and normal-mode splitting function mea-
734 surements. *Geophysical Journal International*, 184(3), 1223–1236. doi:
735 10.1111/j.1365-246X.2010.04884.x

736 Ritsema, J., & Lekić, V. (2020). Heterogeneity of seismic wave velocity in earth’s
737 mantle. *Annual Review of Earth and Planetary Sciences*, 48(Volume 48, 2020),
738 377-401. doi: 10.1146/annurev-earth-082119-065909

739 Rudolph, M. L., Lekić, V., & Lithgow-Bertelloni, C. (2015). Viscosity jump in
740 Earth’s mid-mantle. *Science*, 350(6266), 1349–52. doi: 10.1126/science.aad1929

741 Rudolph, M. L., Moulik, P., & Lekić, V. (2020). Bayesian inference of mantle vis-
742 cosity from whole-mantle density models. *Geochemistry, Geophysics, Geosystems*,
743 21(11), e2020GC009335. doi: 10.1029/2020GC009335

744 Sambridge, M., Bodin, T., Gallagher, K., & Tkalcic, H. (2013). Transdimensional
745 inference in the geosciences. *Phil. Trans. R. Soc. A.*, 371. doi: 10.1098/rsta.2011
746 .0547

747 Saria, E. E., Calais, E., Altamimi, Z., Willis, P., & Farah, H. (2013). A new velocity
748 field for Africa from combined GPS and DORIS space geodetic Solutions: Con-
749 tribution to the definition of the African reference frame (AFREF). *Journal of*
750 *Geophysical Research: Solid Earth*, 118(4), 1677–1697. doi: 10.1002/jgrb.50137

751 Save, H., Bettadpur, S., & Tapley, B. D. (2016). High-resolution CSR GRACE RL05
752 mascons. *Journal of Geophysical Research: Solid Earth*, 121(10), 7547-7569. doi:
753 10.1002/2016JB013007

754 Simmons, N. A., Forte, A. M., & Grand, S. P. (2007). Thermochemical structure
755 and dynamics of the African superplume. *Geophysical Research Letters*, 34(2),
756 L02301. doi: 10.1029/2006GL028009

757 Simmons, N. A., Forte, A. M., & Grand, S. P. (2009). Joint seismic, geody-
758 namic and mineral physical constraints on three-dimensional mantle hetero-
759 geneity: Implications for the relative importance of thermal versus composi-
760 tional heterogeneity. *Geophysical Journal International*, 177(3), 1284-1304. doi:
761 10.1111/j.1365-246X.2009.04133.x

762 Simons, F. J. (2010). Slepian functions and their use in signal estimation and spec-
763 tral analysis. In W. Freedman, M. Z. Nashed, & T. Sonar (Eds.), *Handbook of geo-*
764 *mathematics* (p. 891-923). Springer-Verlag. doi: 10.1007/978-3-642-01546-5_30

765 Simons, F. J., Dahlen, F. A., & Wiczeorek, M. A. (2006). Spatiospectral Concentra-

766 tion on a Sphere. *Society for Industrial and Applied Mathematics*, 48(3), 504–536.
767 doi: 10.1137/S0036144504445765

768 Steinberger, B., Conrad, C. P., Osei Tutu, A., & Hoggard, M. J. (2017). On the am-
769 plitude of dynamic topography at spherical harmonic degree two. *Tectonophysics*.
770 doi: 10.1016/J.TECTO.2017.11.032

771 Sun, M., Fu, X., Liu, K. H., & Gao, S. S. (2018). Absence of thermal influence from
772 the African Superswell and cratonic keels on the mantle transition zone beneath
773 southern Africa: Evidence from receiver function imaging. *Earth and Planetary*
774 *Science Letters*, 503, 108–117. doi: 10.1016/J.EPSL.2018.09.012

775 Wahr, J., Molenaar, M., & Bryan, F. (1998, December). Time variability of the
776 Earth’s gravity field: Hydrological and oceanic effects and their possible detection
777 using GRACE. *J. Geophys. Res.*, 103(B12), 30205–30229.

778 Walford, H. L., & White, N. J. (2005). Constraining uplift and denudation of west
779 African continental margin by inversion of stacking velocity data. *Journal of Geo-*
780 *physical Research: Solid Earth*, 110(B4). doi: 10.1029/2003JB002893

781 Wessel, P., Smith, W. H. F., Scharroo, R., Luis, J., & Wobbe, F. (2013). Generic
782 mapping tools: Improved version released. *Eos, Transactions American Geophys-*
783 *ical Union*, 94(45), 409–410. doi: 10.1002/2013EO450001

784 Wieczorek, M. A., & Simons, F. J. (2005). Localized spectral analysis on the sphere.
785 *Geophys. J. Int.*, 162, 655–675. doi: 10.1111/j.1365-246X.2005.02687.x

786 Yang, T., & Gurnis, M. (2016). Dynamic topography, gravity and the role of lateral
787 viscosity variations from inversion of global mantle flow. *Geophysical Journal In-*
788 *ternational*, 207(2), 1186–1202. doi: 10.1093/gji/ggw335

789 Zhang, N., Zhong, S., & Flowers, R. M. (2012). Predicting and testing continental
790 vertical motion histories since the Paleozoic. *Earth and Planetary Science Letters*,
791 317–318, 426–435. doi: 10.1016/J.EPSL.2011.10.041

792 **Supporting Information for “The influence of mantle**
793 **structure on dynamic topography in southern Africa”**

794 **Kenneth C. Gourley¹ and Christopher Harig¹**

795 ¹Department of Geosciences, University of Arizona, Tucson, AZ, USA

796 **Contents of this file**

- 797 1. Figures S1 to S7

798 **Introduction** We include here three additional viscosity ensemble distribution plots and
799 three additional predicted dynamic topography plots, similar in style to Figures 3 and
800 4, respectively, for each of the following seismic tomography models: SEMUCB-WM1,
801 SAW642ANb, and S362WMANI+M. We also include the vertical displacement uncer-
802 tainty corresponding to Figure 5 for a total of seven supplementary figures.

Figure S1.

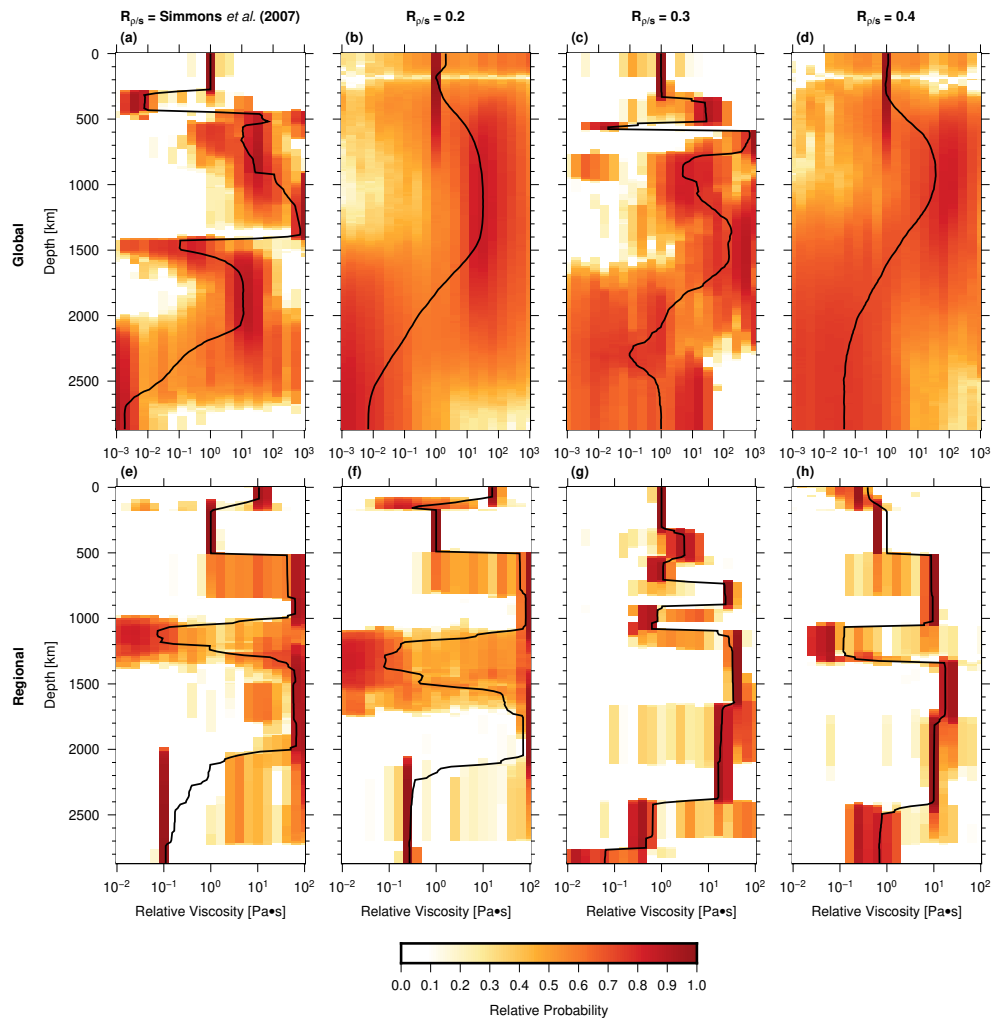


Figure S1. Viscosity inversion ensemble results for tomography model SEMUCB-WM1. Plot panels follow the same formatting as in Figure 3.

Figure S2.

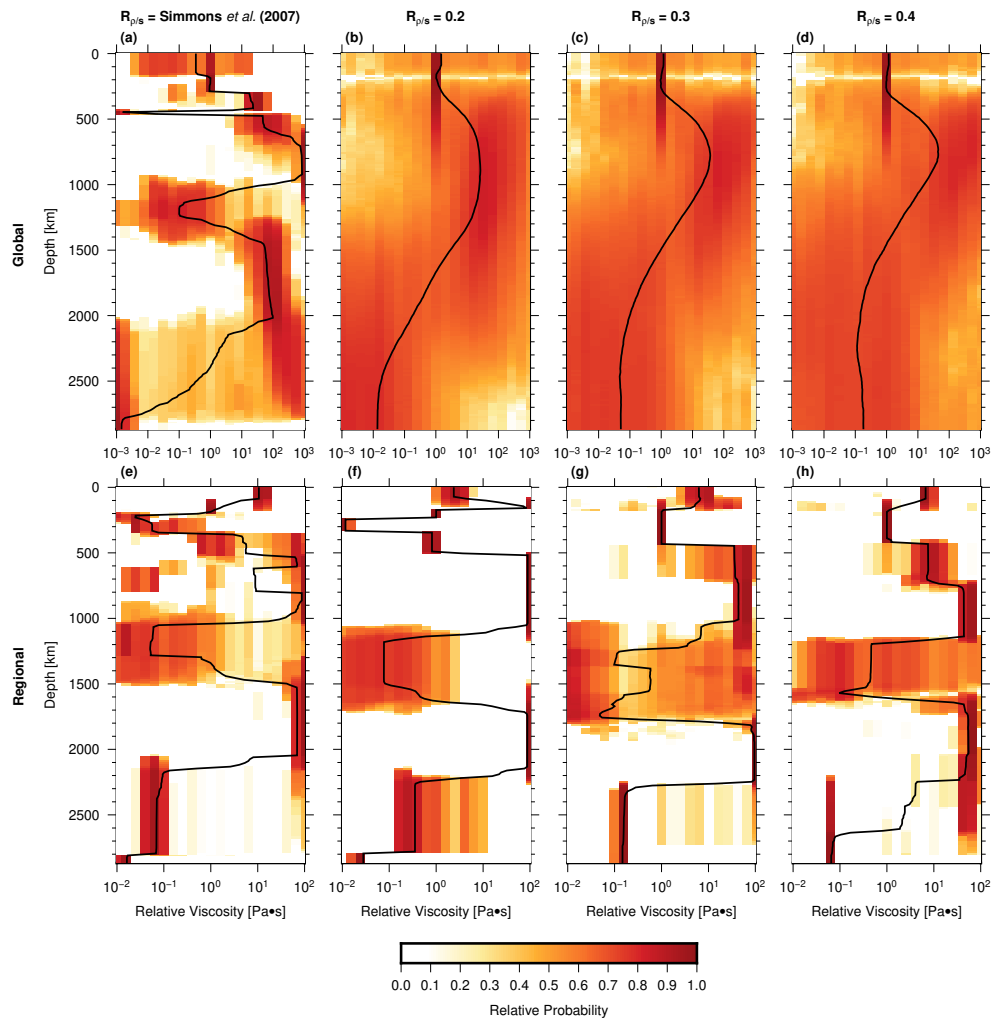


Figure S2. Viscosity inversion ensemble results for tomography model SAW642ANb. Plot panels follow the same formatting as in Figure 3.

Figure S3.

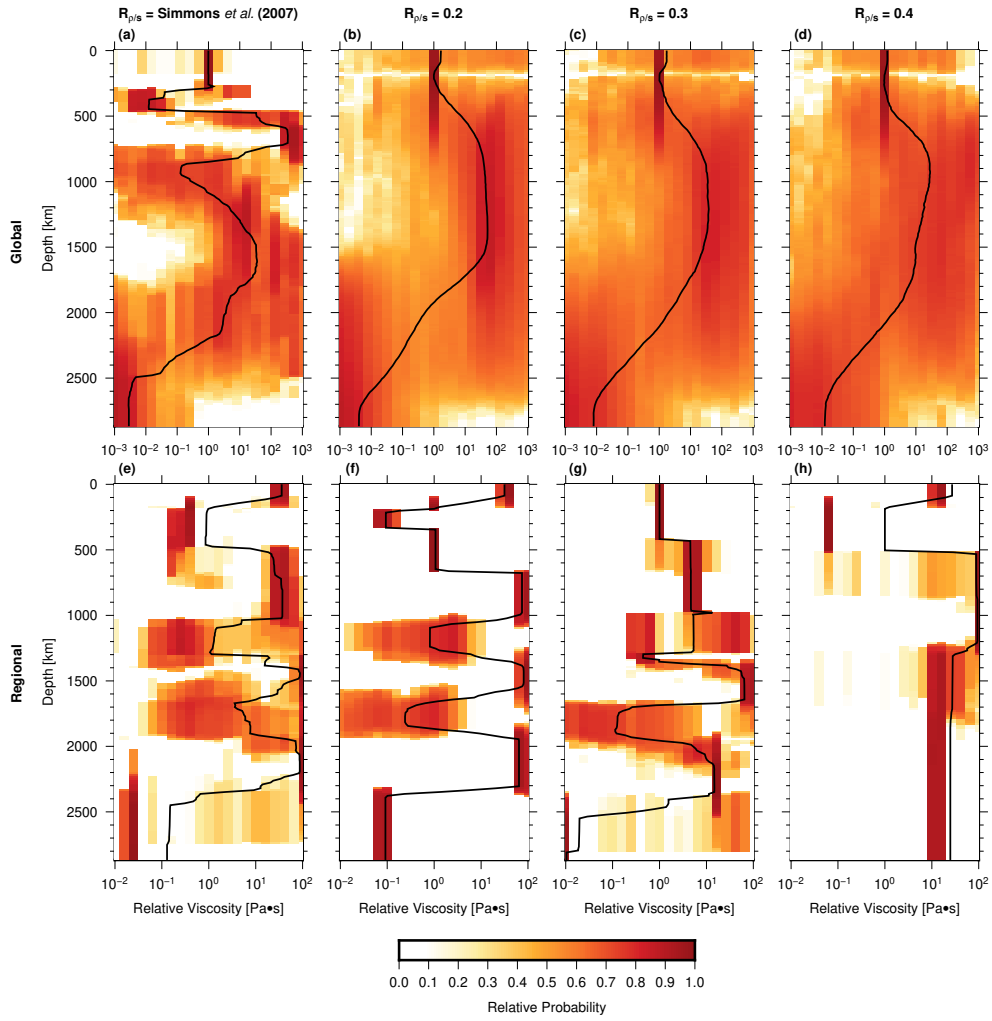


Figure S3. Viscosity inversion ensemble results for tomography model S362WMANI+M. Plot panels follow the same formatting as in Figure 3.

Figure S4.

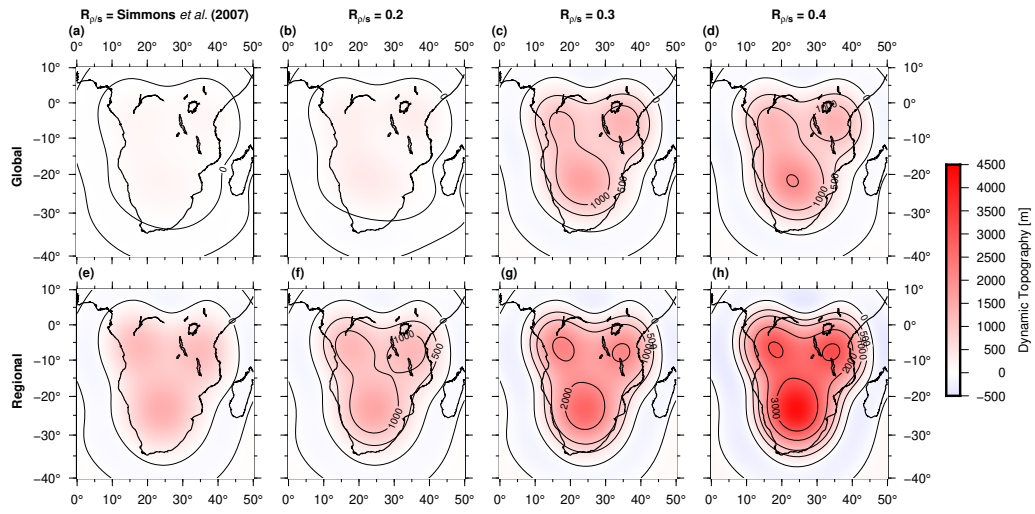


Figure S4. Predicted dynamic topography for tomography model SEMUCB-WM1. Plot panels follow the same formatting as in Figure 4.

Figure S5.

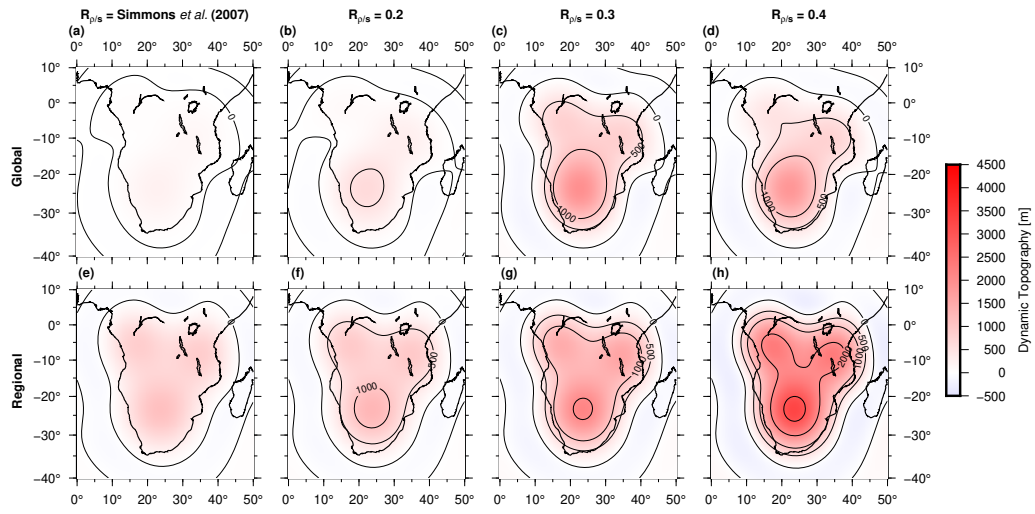


Figure S5. Predicted dynamic topography for tomography model SAW642ANb. Plot panels follow the same formatting as in Figure 4.

Figure S6.

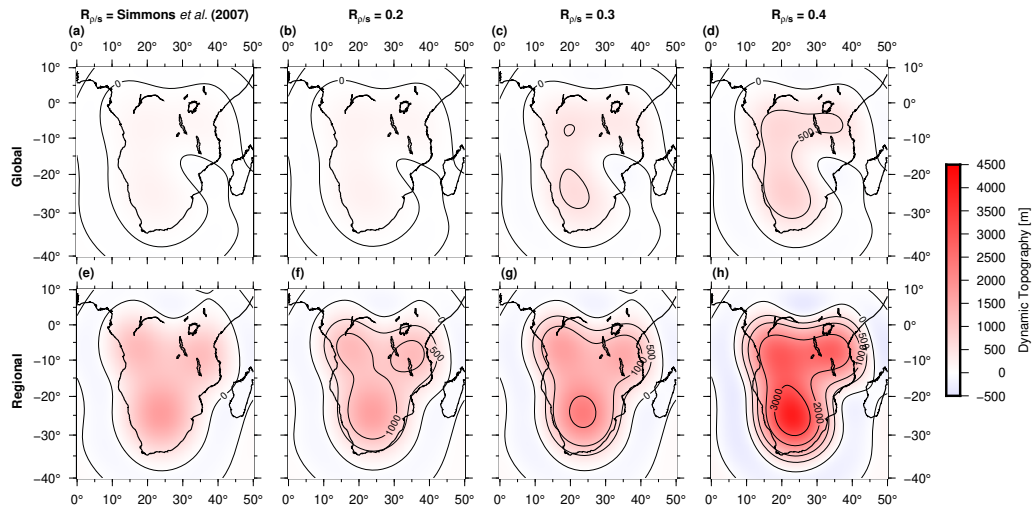


Figure S6. Predicted dynamic topography for tomography model S362WMANI+M. Plot panels follow the same formatting as in Figure 4.

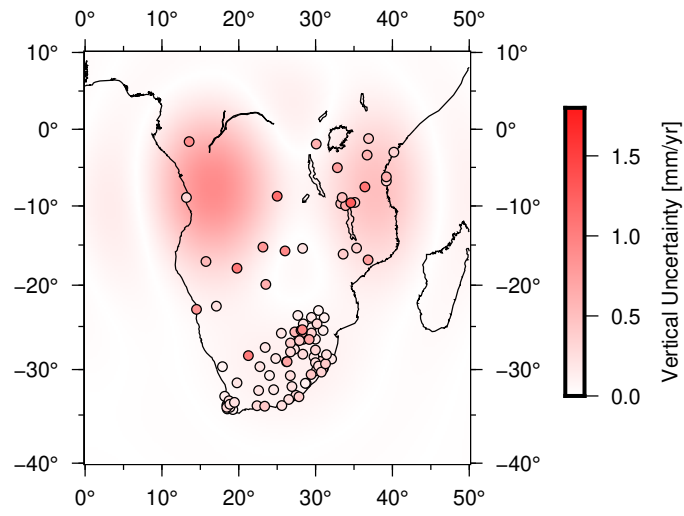
Figure S7.

Figure S7. Long term vertical rate uncertainty from GNSS within our study region. Individual station uncertainties are plotted as filled circles. The localized regional uncertainty is plotted as a color gradient. Areas in the northern part of our region have the highest velocity amplitudes as well as the highest uncertainties due to the poor station coverage in these areas.